



Yolk-shell structured $\text{Fe}_3\text{O}_4@\text{void@TiO}_2$ as a photo-Fenton-like catalyst for the extremely efficient elimination of tetracycline

Dan Du, Wen Shi, Lingzhi Wang*, Jinlong Zhang*

Key Lab for Advanced Materials and Institute of Fine Chemicals, School of Chemistry and Molecular Engineering, East China University of Science and Technology, Shanghai, 200237, PR China

ARTICLE INFO

Article history:

Received 10 May 2016

Received in revised form 18 July 2016

Accepted 25 July 2016

Available online 25 July 2016

Keywords:

Photo-Fenton

$\text{Fe}_3\text{O}_4@\text{void@TiO}_2$

Yolk-shell

TC degradation

ABSTRACT

Herein, we demonstrate the yolk-shell structured $\text{Fe}_3\text{O}_4@\text{void@TiO}_2$ sphere as an efficient heterogeneous catalyst for the photo-Fenton-like degradation of tetracycline (TC). The composite was synthesized by first successively coating amorphous SiO_2 and TiO_2 shells around a Fe_3O_4 core via the sol-gel strategy to form $\text{Fe}_3\text{O}_4@\text{SiO}_2@\text{TiO}_2$, then crystallizing TiO_2 and removing SiO_2 through calcination and the ultrasonic ammonia-etching treatment, respectively. The particles are monodisperse and uniform in size (ca. 180 nm), where the diameter of the core is ca. 100 nm and the thickness of the shell is ca. 10 nm. This composite possesses anatase TiO_2 shell with high crystallinity, superparamagnetic core with a saturation magnetization value of 28.71 emu/g and high specific surface area of 101 m² g⁻¹. It shows extremely high activity towards the degradation of TC (40 mg/L) in a wide pH range as demonstrated by almost 100% elimination efficiency at pH = 3 and ca. 75% at pH = 9 within 6 min. Moreover, benefitting from the superparamagnetism of the core, this composite could be magnetically recovered and reapplied in the TC degradation without significant loss of activity after 5 recycling (ca. 10%). The degradation curve can be well fitted by pseudo-first order model, where a kinetic constant of 0.51 min⁻¹ is achieved, much higher than those of $\text{Fe}_3\text{O}_4@\text{TiO}_2$ (0.24 min⁻¹), hollow TiO_2 (0.17 min⁻¹), $\text{Fe}_3\text{O}_4@\text{SiO}_2@\text{TiO}_2$ (0.14 min⁻¹) and Fe_3O_4 (0.11 min⁻¹). The high activity is attributed to the efficient enrichment and confinement of reactants (TC and hydroxyl radicals) in the nanocavity of the yolk-shell structure, and the efficient reduction of Fe^{3+} to Fe^{2+} by the photo-generated electrons from the TiO_2 shell.

© 2016 Elsevier B.V. All rights reserved.

1. Introduction

Fenton and photo-Fenton reactions, as a typical advanced oxidation process (AOP), utilizing Fe^{2+} and H_2O_2 to produce hydroxyl radicals ($\cdot\text{OH}$) with an extremely high oxidation potential of 2.8 V vs. NHE, are particularly useful for eliminating biologically toxic or non-degradable organics such as pesticides, pharmaceuticals, volatile organic compounds and petroleum in waste water and contaminated soils. In the context of treatment of pharmaceutical wastewaters [1,2], the effective removal of antibiotics from manufacturing plants and hospitals has become a worldwide concern due to the wide variety of components, broad range of concentrations and difficulty of metabolism by animals, which are finally ended up in the wastewater system and widely detected in soils, surface waters, ground water, coastal environment, and even drinking water [3,4].

As such, Fenton technology for the decontamination of antibiotics with a wide working pH range and easy recoverability is extremely desirable, which has emerged as an important topic during the last decade [5]. TC is one of the most widely used antibiotics worldwide, and is difficult to be metabolized in animals. Homogeneous Fenton systems which are based on ferrous ion and hydrogen peroxide are proven to be effective technologies for destruction of TC [6]. Limitations of Fenton-based AOP in wastewater treatment stem mainly from the need for pH control and the problem of sludge generation [7,8]. The heterogeneous Fenton reaction eliminates the sludge disposal problems in the classic Fenton reaction by using recyclable catalyst, and can be performed in neutral pH range [9,10], which has been applied to remove TC from contaminated water resources pollutants [5,11]. However, due to the decreased degradation rates and the remained large consumption of H_2O_2 , great efforts to improve the heterogeneous Fenton efficiency still need to be made by catalyst design and modification, which has currently attracted extensive attention. The low oxidation efficiency of the heterogeneous Fenton reaction could be due to the decreased oxidation potential of $\cdot\text{OH}$ with increasing pH. Moreover, the reduc-

* Corresponding author.

E-mail addresses: wlz@ecust.edu.cn (L. Wang), jlzhang@ecust.edu.cn (J. Zhang).

tion of solid Fe^{3+} at high pH is much slower than that of aqueous Fe^{3+} at low pH [12,13]. The catalytic activity of a heterogeneous Fenton catalyst is thus mainly dependent on its electron transfer ability. Recently, some binary complexes composed of Fe-base compound and other semiconductors in the form of core@shell or loading have proved to be effective on improving the photo-Fenton activity, mainly due to the sustainable reduction of Fe^{3+} to Fe^{2+} by the photo-induced electron generated from the semiconductor [14–16].

As a novel class of complex nanostructures, yolk-shell structured materials with a typical core@void@shell architecture have received considerable attention [17,18]. With the appealing structures of movable cores, interstitial hollow spaces and multifunctional shells, this kind of material plays an important role in modern science and technology as potential candidates for tremendous applications such as confined catalysis [19–21], lithium-ion batteries [22,23], drug delivery [24–26], and sensors [27]. In particular, this nanostructure shows promise for applications as a nanoreactor for several important reactions because of its permeable shell can protect the core from aggregation while allowing the diffusion of small active molecules in and out of the interior microenvironment. To the best of our knowledge, no study so far has succeeded in designing yolk-shell nanostructures with two semiconductors for the heterogeneous photo-Fenton-like process.

Recently, TiO_2 coupled with iron oxide has been reported to have a good magnetic response and displayed a high photocatalytic efficiency [28,29]. In this work, we have successfully synthesized the yolk-shell structured $\text{Fe}_3\text{O}_4@\text{void}@\text{TiO}_2$ NPs composed of a movable superparamagnetic Fe_3O_4 core (ca. 100 nm) and anatase TiO_2 shell (ca. 10 nm), which was applied to the photo-Fenton-like degradation of TC as a model antibiotics contaminant. The effects of various operational parameters including concentrations of catalyst and H_2O_2 , and pH value on the degradation efficiency of TC, as well as the reusability of the catalyst were systematically evaluated. Extraordinarily high and stable catalytic activity has been achieved on $\text{Fe}_3\text{O}_4@\text{void}@\text{TiO}_2$ with a wide working pH range of 3–9. The enrichment and confinement of TC and photo-induced $\cdot\text{OH}$ in the nanocavity, as well as the effective recycling between Fe^{2+} and Fe^{3+} pumped by the TiO_2 shell is responsible for the excellent activity according to a variety of controlled photo-Fenton-like experiments conducted on Fe_3O_4 , $\text{Fe}_3\text{O}_4@\text{TiO}_2$, $\text{Fe}_3\text{O}_4@\text{SiO}_2@\text{TiO}_2$ and hollow TiO_2 .

2. Experimental

2.1. Chemicals

Ferric chloride hexahydrate ($\text{FeCl}_3 \cdot 6\text{H}_2\text{O}$), sodium acetate (NaAc), trisodium citrate, ethylene glycol, tetraethyl orthosilicate (TEOS), ethanol, hydrogen peroxide (H_2O_2), *tert*-butyloxide (TBOT), ammonia aqueous solution ($\text{NH}_3 \cdot \text{H}_2\text{O}$, 28 w%), *tert*-butyl alcohol (TBA), silver nitrate (AgNO_3), *p*-benzoquinone (BQ), ammonium oxalate (AO), Tetracycline (TC) hydrochloride were obtained from Aladdin. All chemicals were of analytical grade, and they were used without further purification.

2.2. Preparation for different NPs

Synthesis of magnetite Fe_3O_4 NPs. The water dispersible Fe_3O_4 NPs were synthesized according to the method reported previously [30]. Briefly, $\text{FeCl}_3 \cdot 6\text{H}_2\text{O}$ (4.30 g), trisodium citrate (2.35 g), and sodium acetate (NaAc , 8.75 g) were dissolved in ethylene glycol (150 mL) with a mechanical stirring. Then, the obtained yellow solution was transferred and sealed into a Teflon-lined stainless-steel autoclave. The autoclave was heated at 200 °C for 10 h, and then cooled down to room temperature. The black magnetic prod-

ucts were washed with deionized water and ethanol for three times, respectively.

Synthesis of $\text{Fe}_3\text{O}_4@\text{SiO}_2$ NPs. The core-shell $\text{Fe}_3\text{O}_4@\text{SiO}_2$ NPs were prepared through a versatile sol-gel method as follows [31]: the Fe_3O_4 magnetite particles (50 mg) was added to a three-neck round-bottom flask charged with absolute ethanol (200 mL), deionized water (50 mL) and concentrated ammonia solution (3.5 mL, 28 wt%) under ultrasound for 15 min, then stirred for 1 h. Afterward, 0.3 mL of TEOS was added dropwise in 10 min. Then the mixed solution was stirred for 10 h at room temperature. The resultant core-shell $\text{Fe}_3\text{O}_4@\text{SiO}_2$ NPs products were separated and collected with a magnet, followed by washing with deionized water and ethanol for three times, respectively.

Synthesis of $\text{Fe}_3\text{O}_4@\text{SiO}_2@\text{TiO}_2$ NPs. The core-shell $\text{Fe}_3\text{O}_4@\text{SiO}_2@\text{TiO}_2$ NPs were synthesized based on the hydrolysis and condensation of TBOT [32]. The above obtained $\text{Fe}_3\text{O}_4@\text{SiO}_2$ NPs (0.15 g) were dispersed in ethanol (200 mL), and mixed with concentrated ammonia solution (0.9 mL, 28 wt%) under ultrasound for 15 min. Afterward, 2.0 mL of TBOT was added dropwise in 5 min, and the reaction was allowed to proceed for 24 h at 45 °C under mechanical stirring. The resultant product was separated and collected with a magnet, followed by washing with deionized water and ethanol for 3 times, respectively. $\text{Fe}_3\text{O}_4@\text{SiO}_2@\text{TiO}_2$ NPs were calcined in N_2 atmosphere at 450 °C for 2 h to crystallize the amorphous TiO_2 . The yolk-shell structured $\text{Fe}_3\text{O}_4@\text{void}@\text{TiO}_2$ were synthesized by mild ultrasonic treatment in ammonia solution (0.1 M) for 1 h. The final product was separated and collected with a magnet. Then the samples were washed and dried at 60 °C thoroughly in vacuum oven.

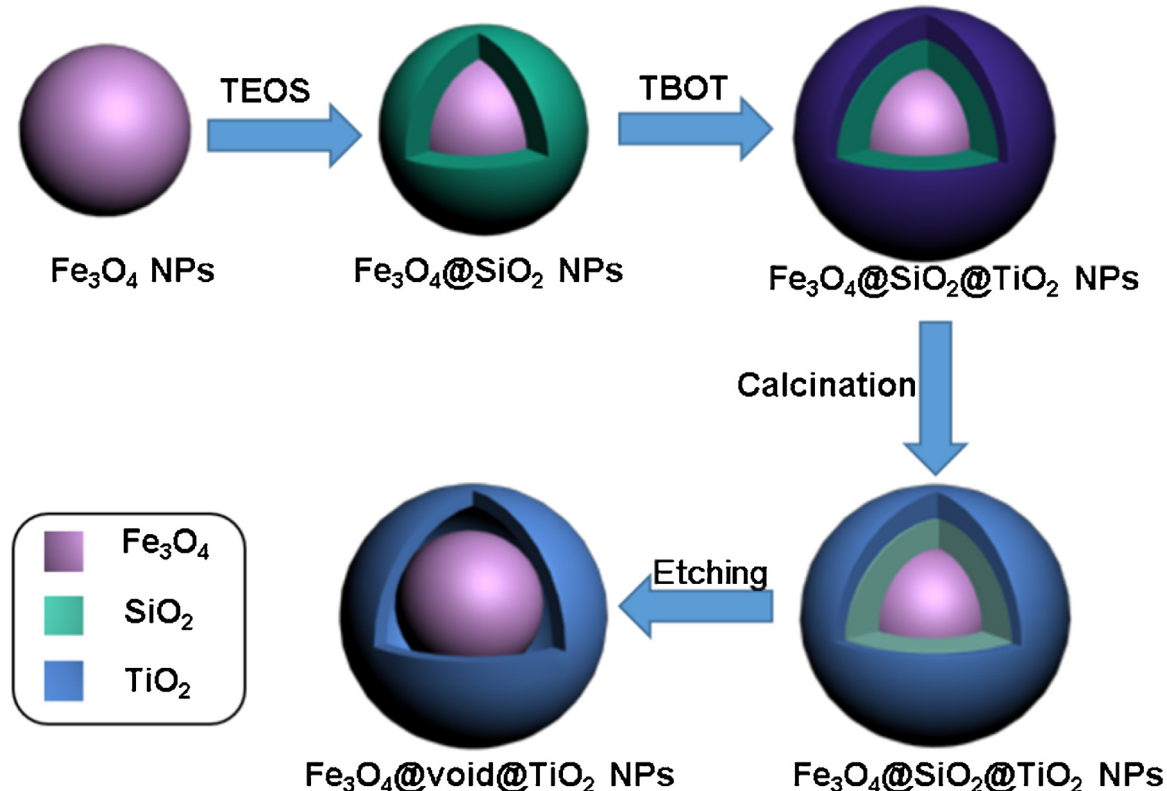
Synthesis of $\text{Fe}_3\text{O}_4@\text{TiO}_2$ and hollow TiO_2 NPs. The preparation procedure for $\text{Fe}_3\text{O}_4@\text{TiO}_2$ NPs was similar to $\text{Fe}_3\text{O}_4@\text{SiO}_2@\text{TiO}_2$ NPs. It is convenient to get $\text{Fe}_3\text{O}_4@\text{TiO}_2$ that use Fe_3O_4 NPs as the core coated with TiO_2 and a further calcination was conducted later. As for hollow TiO_2 NPs, the SiO_2 NPs synthesized from classical Stöber method [33] with the diameter of ~150 nm were used as the template. After coated with TiO_2 shell, the hollow TiO_2 NPs were generated by etching method.

2.3. Catalytic activity test

The as-prepared catalyst was evaluated by photodegradation of TC in aqueous solution under UV irradiation. All catalytic reactions were conducted in quartz tube with constant stirring. Typically, 10 mg of $\text{Fe}_3\text{O}_4@\text{void}@\text{TiO}_2$ was added into the 40 mL aqueous solution containing 40 mg/L TC. The suspension without H_2O_2 was stirred in dark for 30 min to reach adsorption-desorption equilibrium between the catalysts and TC. Then the photo-Fenton-like reaction was carried out by adding a certain amount of H_2O_2 to the solution, which was irradiated by a 300 W Xenon lamp with a whole spectrum (200–1000 nm). The light intensity of the Xenon lamp in the center of the TC solution was 345 mW cm⁻². Aliquots were collected at given time intervals and catalysts were separated by magnetic separation. The concentration of the remnant TC was determined by testing the absorbance of the supernatant at 357 nm with UV-vis spectroscopy.

2.4. Characterizations

TEM images were conducted with a JEOL JEM 2010F electron microscope instrument operating at 200 kV. X-ray powder diffraction (XRD) patterns were obtained with a Rigaku D/max 2550 VB/PC apparatus. The Brunauer–Emmett–Teller (BET) surface area and pore-size distribution were measured by N_2 adsorption and desorption by using a Micromeritics ASAP 2020 instrument. UV/Vis absorption spectra were measured with a Shimadzu 2450 spectrophotometer. The electron spin resonance (ESR) technique



Scheme 1. Schematic illustration of the formation procedure of the yolk-shell structured $\text{Fe}_3\text{O}_4@\text{void}@\text{TiO}_2$ NPs.

(with DMPO) was employed to detect the radical species over the photo-Fenton-like system on a Bruker EMX-8/2.7 spectrometer. The system was irradiated by using 300 W Xenon lamp and immediately mixed with DMPO. The magnetic hysteresis loop was measured by a vibrating sample magnetometer (VSM, LakeShore 7407) at room temperature.

3. Results and discussion

3.1. Synthesis methods and characterizations

The typical synthesis of yolk-shell structured $\text{Fe}_3\text{O}_4@\text{void}@\text{TiO}_2$ NPs is depicted in Scheme 1. First, the pre-synthesized magnetic Fe_3O_4 NPs were coated with a nonporous silica layer through a sol-gel approach in the presence of tetraethyl orthosilicate (TEOS) (denoted as $\text{Fe}_3\text{O}_4@\text{SiO}_2$). Then, a further sol-gel coating process was utilized to deposit a porous TiO_2 shell onto the nonporous silica layer using tetrabutyl titanate (TBOT) as the precursor ($\text{Fe}_3\text{O}_4@\text{SiO}_2@\text{TiO}_2$) [32], followed by a calcination at 450 °C in N_2 atmosphere. Finally, an ultrasound-assisted etching method was used to etch off the nonporous silica layer in a weak alkaline media to the resultant $\text{Fe}_3\text{O}_4@\text{void}@\text{TiO}_2$. The transmission electron microscope images (TEM) reveal that the obtained Fe_3O_4 NPs (Fig. 1a) have a fairly uniform diameter of ca. 120 nm. After the first sol-gel process, the magnetite microspheres were coated with a silica layer with a thickness of ca. 25 nm (Fig. 1a). The further sol-gel process leads to the formation of $\text{Fe}_3\text{O}_4@\text{SiO}_2@\text{TiO}_2$ NPs (Fig. 1b) with a diameter of ca. 180 nm, indicating the presence of ca. 5 nm thick TiO_2 layer. After a further coating process, the $\text{Fe}_3\text{O}_4@\text{SiO}_2@\text{TiO}_2$ composites were calcined at 450 °C in N_2 for 2 h to crystallize TiO_2 . Subsequently, the sonication of $\text{Fe}_3\text{O}_4@\text{SiO}_2@\text{TiO}_2$ for 1 h in 0.1 M ammonia hydroxide solution resulted in hollow yolk-shell structured $\text{Fe}_3\text{O}_4@\text{void}@\text{TiO}_2$ (Fig. 1c, d) at room temperature. After the process of calcination and etch-

ing, the diameter of the Fe_3O_4 core shrinks to ca. 100 nm while the TiO_2 shell increases to ca. 10 nm. The high-resolution TEM image reveals lattice fringes of the core with an interplanar spacing value of 0.49 nm (Fig. 1e), which are in good agreement with the values of the (111) planes of cubic phase Fe_3O_4 [34]. As represented in Fig. 1f, the lattice fringes of the shell are measured to be 0.35 nm, analogous to the (101) planes of anatase TiO_2 [35]. The similar synthesis procedures were conducted to prepare $\text{Fe}_3\text{O}_4@\text{TiO}_2$ and hollow TiO_2 NPs. The microstructures of these two kinds of NPs are presented in Fig. S1.

The powder X-ray diffraction (PXRD) pattern of the Fe_3O_4 NPs shows a typical cubic structure of Fe_3O_4 (JCPDS card No. 19-0629, Fig. 2a) [36]. New characteristic peaks indexed to the anatase phase of TiO_2 (JCPDS card no. 21-1272) are revealed from $\text{Fe}_3\text{O}_4@\text{SiO}_2@\text{TiO}_2$. In addition, a broad peak attributed to the amorphous SiO_2 is clearly observed in the range of 20–28°, which disappears after etching of SiO_2 layer with ammonia [37]. The BET surface area of the Fe_3O_4 NPs was calculated to be 68 $\text{m}^2 \text{g}^{-1}$ from N_2 sorption isotherms based on Brunauer–Emmett–Teller (BET) method (Fig. 2b). After coating with SiO_2 and TiO_2 , the surface area of $\text{Fe}_3\text{O}_4@\text{SiO}_2@\text{TiO}_2$ NPs decreases to 51 $\text{m}^2 \text{g}^{-1}$. A typical type IV curve with a hysteresis loop at relative pressure from 0.80 to 1.00 can be observed after the ammonia treatment of $\text{Fe}_3\text{O}_4@\text{SiO}_2@\text{TiO}_2$, suggesting the formation of hollow cavity. The specific surface area increases to 101 $\text{m}^2 \text{g}^{-1}$ for sample $\text{Fe}_3\text{O}_4@\text{void}@\text{TiO}_2$. The saturation magnetization value of pure $\text{Fe}_3\text{O}_4@\text{void}@\text{TiO}_2$ NPs was measured to be 28.71 emu/g (Fig. 3), weaker than that of pure Fe_3O_4 (42.15 emu/g), which could be ascribed to the existence of TiO_2 shell.

3.2. Adsorption behavior of TC on $\text{Fe}_3\text{O}_4@\text{void}@\text{TiO}_2$

With the frequent consumption for human domestic or hospital use and veterinary and agriculture purposes, antibiotics have

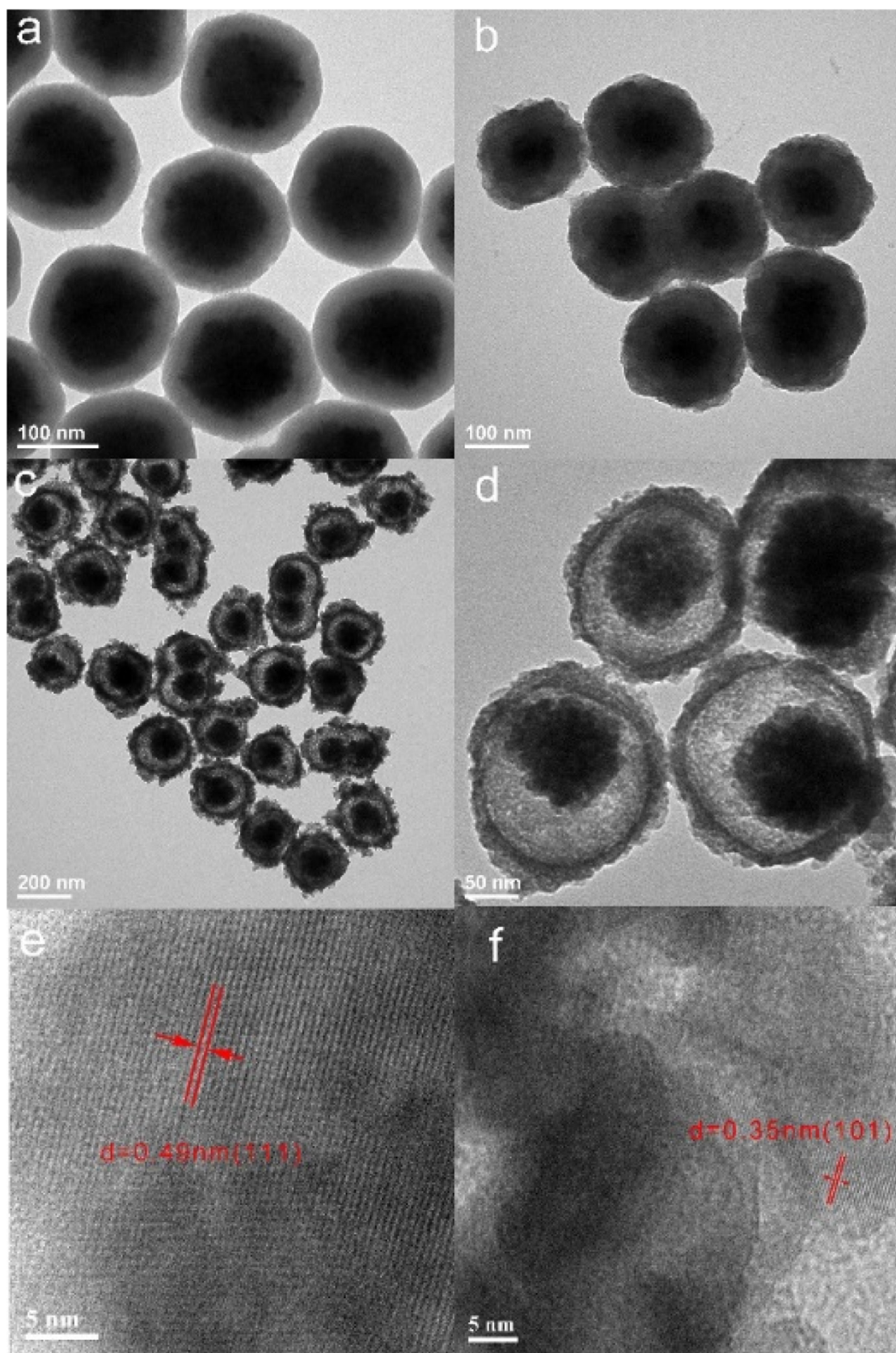


Fig. 1. TEM images: (a) Fe₃O₄@SiO₂, (b) Fe₃O₄@SiO₂@TiO₂, (c, d) yolk-shell structured Fe₃O₄@void@TiO₂ NPs. HRTEM images: (e) the Fe₃O₄ core, (f) the TiO₂ shell.

been continuously released into the environment, resulting in a widespread environmental invasion [38]. Herein, TC was selected as the model antibiotics contaminant to investigate the catalytic

activity of as-prepared Fe₃O₄@void@TiO₂ composite as a Fenton catalyst. As an antibiotic, TC is often detected in the final effluents from wastewater treatment plants [39]. The concentration of TC

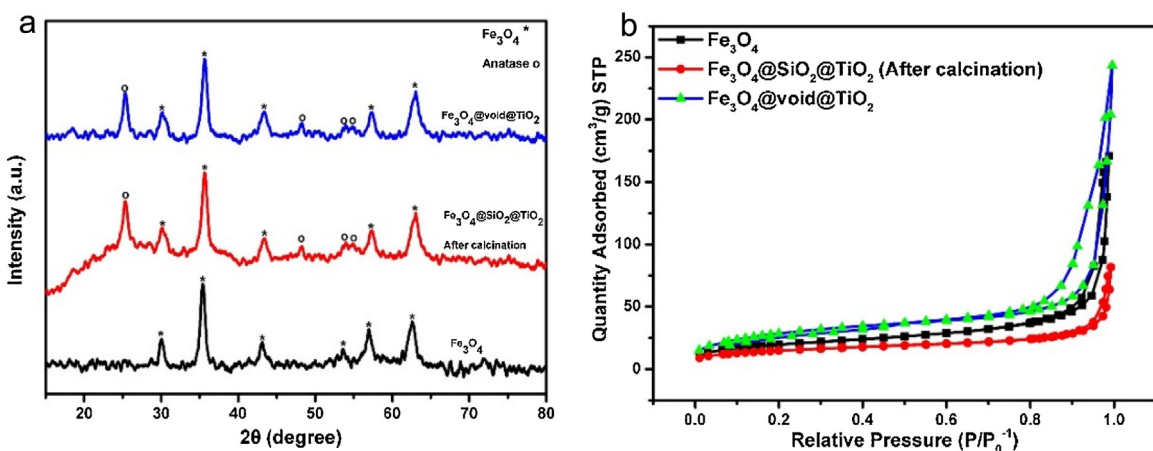


Fig. 2. (a) XRD patterns of bare Fe_3O_4 , $\text{Fe}_3\text{O}_4@\text{SiO}_2@\text{TiO}_2$ and $\text{Fe}_3\text{O}_4@\text{void}@{\text{TiO}}_2$ NPs. (b) N_2 sorption isotherms of bare Fe_3O_4 , $\text{Fe}_3\text{O}_4@\text{SiO}_2@\text{TiO}_2$ and $\text{Fe}_3\text{O}_4@\text{void}@{\text{TiO}}_2$ NPs.

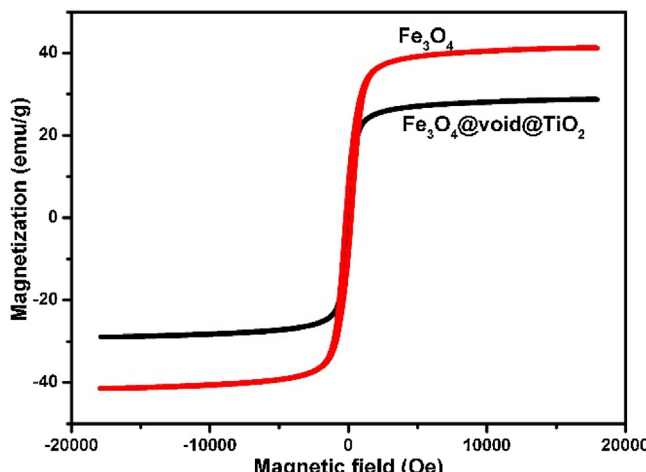


Fig. 3. Magnetic hysteresis loops of Fe_3O_4 and $\text{Fe}_3\text{O}_4@\text{void}@{\text{TiO}}_2$ NPs at room temperature.

was determined by calculating the absorbance at a wavelength of 357 nm (Fig. S2). Before UV irradiation, the suspension containing $\text{Fe}_3\text{O}_4@\text{void}@{\text{TiO}}_2$ NPs and TC were stirred in dark for 30 min to achieve an adsorption-desorption equilibrium.

10 mg $\text{Fe}_3\text{O}_4@\text{void}@{\text{TiO}}_2$ NPs were dispersed in the 40 mL aqueous TC solution of different concentrations (10–60 mg/L). The adsorption equilibrium can be reached within 15 min for an initial TC concentration of 40 mg/L at room temperature (Fig. S3a). The magnetic particles can be separated quickly by an external magnet. The adsorption kinetics data of TC were further fitted by pseudo-second-order kinetic models (Fig. S3b) with a linear coefficient R2 value close to 1 (0.995). After the adsorption equilibrium is reached, ca. 35.7% of the TC is captured. The adsorption ability was further investigated with the initial TC concentration ranging from 10 to 60 mg/L to demonstrate the adsorption thermodynamic behavior which can be fitted by a Langmuir model (Fig. S3c). The calculated maximum adsorption capacity of $\text{Fe}_3\text{O}_4@\text{void}@{\text{TiO}}_2$ is 64.85 mg/g. More parameters were displayed in Table S1 and S2.

According to Zeta potential vs. pH curve (Fig. S4), the isoelectric point (IEP) of $\text{Fe}_3\text{O}_4@\text{void}@{\text{TiO}}_2$ is pH 3.7, which is lower than TiO_2 reported previously (IEP = 6.8) [40]. It means that the $\text{Fe}_3\text{O}_4@\text{void}@{\text{TiO}}_2$ surface is positively charged in acidic solution (pH < 3.7) while negatively charged in relatively basic solution (pH > 3.7). In the present work, an ultrasound-assisted etching method was used to etch off the nonporous silica layer in a weak alkaline media to produce $\text{Fe}_3\text{O}_4@\text{void}@{\text{TiO}}_2$. Patil et al. [41] reported that

the IEP of materials depends on both the synthesis method and the chemicals involved in the synthesis process. The use of alkaline solution led to a material with an IEP of 4.5 whereas acid solution in the last step led to a material with an IEP of 9.5. From the FT-IR spectra (Fig. S5a), the peak at 3400 cm^{-1} is attributed to the stretching vibrations of hydroxyl group, which is assigned to OH^- adsorbed by Fe_3O_4 nanoparticles [42]. TC (Fig. S5b) shows characteristic peaks at 2748 and 2659 cm^{-1} assigned to NHR_3^+ group, 1674 and 1522 cm^{-1} assigned to Amide I and Amide II bands, 1455 cm^{-1} associated to C–C stretching vibration [39]. As for $\text{Fe}_3\text{O}_4@\text{void}@{\text{TiO}}_2$ adsorbed with TC (Fig. S5c), the peak at 1455 cm^{-1} is attributed to the TC. Other peaks of TC was covered with the broad bands of $\text{Fe}_3\text{O}_4@\text{void}@{\text{TiO}}_2$. The existence of non-electrostatic interactions (e.g. H-bond formations) can be inferred due to the polar groups on the surface of TC and $\text{Fe}_3\text{O}_4@\text{void}@{\text{TiO}}_2$.

3.3. Photo-Fenton-like degradation of TC

With the addition of H_2O_2 and illumination, the decreased absorbance peak at 357 nm is used to indicate the decomposition of TC. The effect of the catalyst concentration on the activity was investigated first (Fig. 4a). In the presence of 0.10 g/L catalyst, ca. 80% of TC was degraded within 10 min according to the decreased absorption of TC. The degradation efficiency improves with the increasing catalyst concentration, and almost all of TC is completely degraded within 6 min at a catalyst concentration of 0.25 g/L. A higher concentration of 0.35 g/L does not cause much improvement of the degradation efficiency. Meanwhile, the influence of H_2O_2 concentration (CH_2O_2) was further explored at a catalyst concentration of 0.25 g/L. Only 50% TC is degraded at $\text{CH}_2\text{O}_2 = 0.094$ M. The degradation efficiency is proportional to CH_2O_2 and reaches to a plateau at $\text{CH}_2\text{O}_2 = 0.377$ M (Fig. 4b). Further increase of CH_2O_2 to 0.472 M does not result in an obviously improved efficiency.

The effect of pH is illustrated in Fig. 4c, where the increase of pH value from 3 to 7 causes ca. 10% decrease of the degradation efficiency and ca. 20% decrease at pH = 9 after reaction for 6 min, demonstrating a wide pH working range of this yolk-shell structure. $\text{Fe}_3\text{O}_4@\text{void}@{\text{TiO}}_2$ NPs can be collected from the solution and recycled easily by an external magnetic field. $\text{Fe}_3\text{O}_4@\text{void}@{\text{TiO}}_2$ NPs exhibits an remarkable stability under acid condition after six cycles (Fig. S6) and the concentration of iron leached from the catalyst ranges from 0.95 to 0.88 mg/L (Fig. S7a). Some studies reported that Fe (II) or Fe (III) can exist as aquo-complexes and have chelating activity for tetracycline [43]. In order to evaluate the effect of iron leached from the catalyst, Fe_2SO_4 was selected as the source of Fe^{2+} which is an important reactant in the homogeneous Fenton reac-

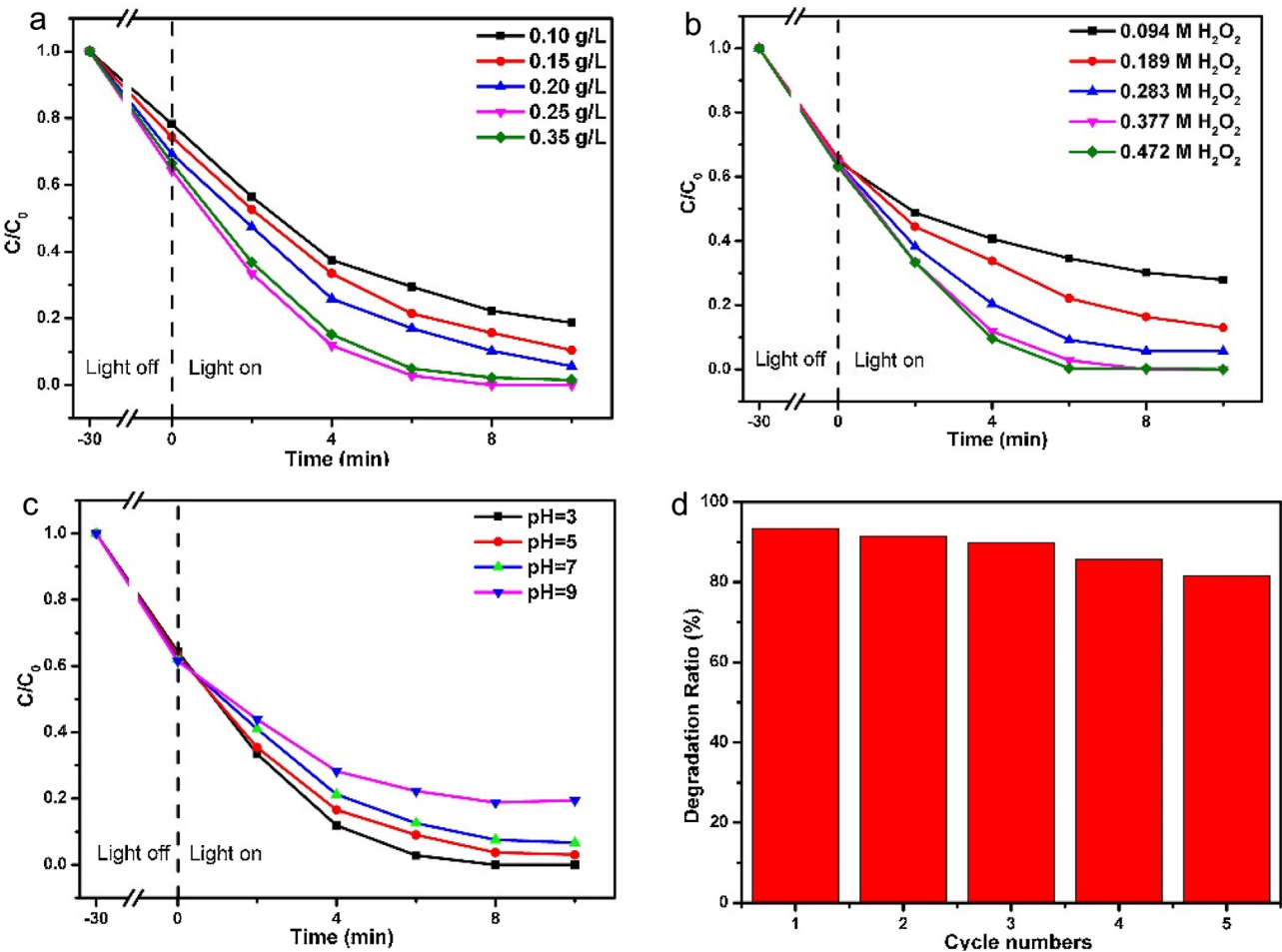


Fig. 4. Photo-Fenton-like degradation of TC. (a) At different concentrations of Fe₃O₄@void@TiO₂ NPs with fixed concentrations of 0.377 M H₂O₂ at pH 3. (b) At different concentrations of H₂O₂ with fixed concentration of 0.25 g/L Fe₃O₄@void@TiO₂ NPs at pH 3. (c) At different pH with fixed concentration of 0.25 g/L Fe₃O₄@void@TiO₂ NPs and 0.377 M H₂O₂. (d) Catalytic behavior of the recycled Fe₃O₄@void@TiO₂ NPs (conditions: 40 mg/L TC, 0.25 g/L Fe₃O₄@void@TiO₂, 0.377 M H₂O₂, pH = 7, reaction time: 10 min, 5 cycles, room temperature).

tion. The concentration of Fe²⁺ in the above reaction is 0.95 mg/L. As shown in Fig. S7b, the degradation ratio is only 75% in 10 min, mainly due to the photolysis of H₂O₂ under UV light. Therefore, the iron ions have little effect on the catalytic efficiency in our reaction system. The mineralization of TC was evaluated by measuring the decay of the total organic carbon (TOC). As exhibited in Fig. S8a, after six runs, the TOC removal efficiency of TC decreased from 26.9% to 22.9%. The TOC removal efficiency could reach 75% with the extension of time (Fig. S8b). The recycle test of the yolk-shell structured Fe₃O₄@void@TiO₂ at pH 7 was also examined (Fig. 4d). The removal efficiency of TC under pH = 7 decreases from 94% to 84% after five recycles, which still remains at ca. 70% even much more cycles with a total irradiation time of ca. 200 h were performed (Fig. S9), demonstrating an excellent stability of the materials under the neutral condition.

To understand the reaction mechanism, a series of control experiments was further carried out. As shown in Fig. 5a, the concentration of TC decreases for ca. 26% in the absence of catalyst (UV/H₂O₂), and ca. 50% without the UV irradiation (Fe₃O₄@void@TiO₂/H₂O₂) within 10 min. The decrease in UV/H₂O₂ system should be attributed to the degradation of TC by •OH decomposed from H₂O₂ under the UV irradiation [44]. In contrast, the decrease in the presence of Fe₃O₄@void@TiO₂ NPs before light irradiation is mostly attributed to the dark adsorption (ca. 40%, 30 min). The further application of UV light immediately results in the total decrease within 6 min, with a negligible contribution of 5% from

the dark adsorption, suggesting the overwhelmingly high elimination efficiency of the photo-Fenton process. When bare Fe₃O₄ NPs is applied as a Fenton-like catalyst, 44% degradation efficiency was achieved within 6 min in the presence of H₂O₂. Moreover, it can be found that the Fe₃O₄@SiO₂@TiO₂ and Fe₃O₄@TiO₂ NPs without cavity shows degradation efficiencies of 62% and 83% respectively. TiO₂ NPs with hollow structure show a degradation ratio of 78%. As a whole, the yolk-shell structured Fe₃O₄@void@TiO₂ NPs exhibit the highest catalytic activity than those of bare Fe₃O₄, TiO₂ and Fe₃O₄@TiO₂ NPs. The degradation kinetic curves can be expressed as the pseudo-first order model as follows:

$$-\ln(C/C_0) = kt + b$$

where *k* is the pseudo-first order rate constant, C₀ is the initial concentration, C is the concentration at time *t*, respectively. As shown in Fig. S10, the *k* value of Fe₃O₄@void@TiO₂ is calculated to be 0.51 min⁻¹, which is much higher than those of Fe₃O₄@SiO₂@TiO₂ (0.14 min⁻¹), Fe₃O₄@TiO₂ (0.24 min⁻¹), Fe₃O₄ (0.11 min⁻¹) and hollow TiO₂ (0.17 min⁻¹).

The ESR technique was further employed to test active radicals using 5, 5-dimethyl-1-pyrroline N-oxide (DMPO) as the spin trapper. As shown in Fig. 6, the typical 4-fold peaks of DMPO-•OH observed in the ESR spectrum with an intensity ratio of 1:2:2:1 clearly confirm that the •OH radicals were formed in Fe₃O₄@void@TiO₂. To determine the main reactive species responsible for the degradation of TC over Fe₃O₄@void@TiO₂ catalysts,

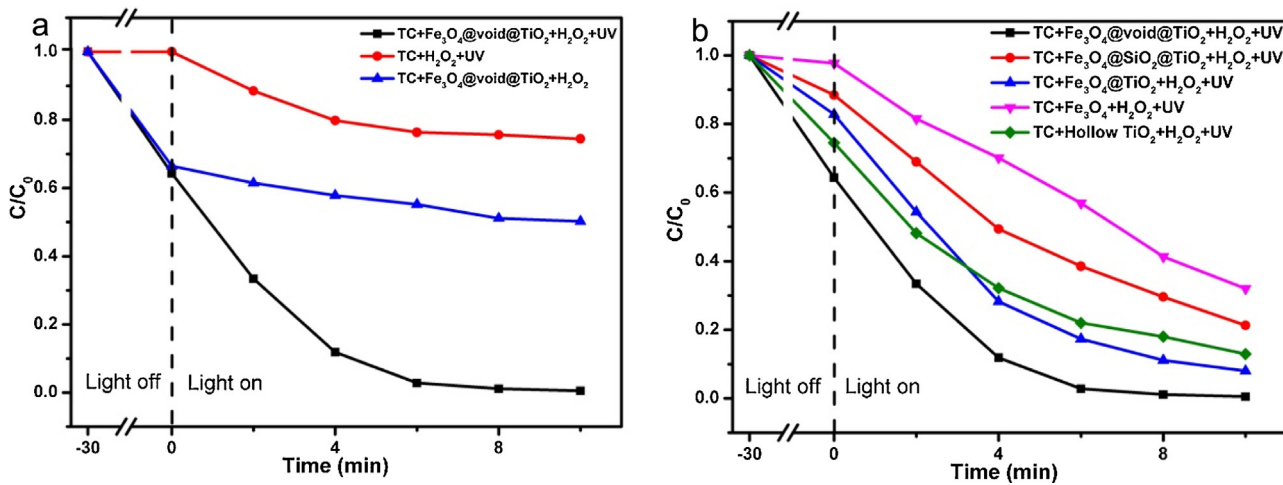


Fig. 5. Photo-Fenton-like degradation of TC at room temperature and pH 3 under different conditions.

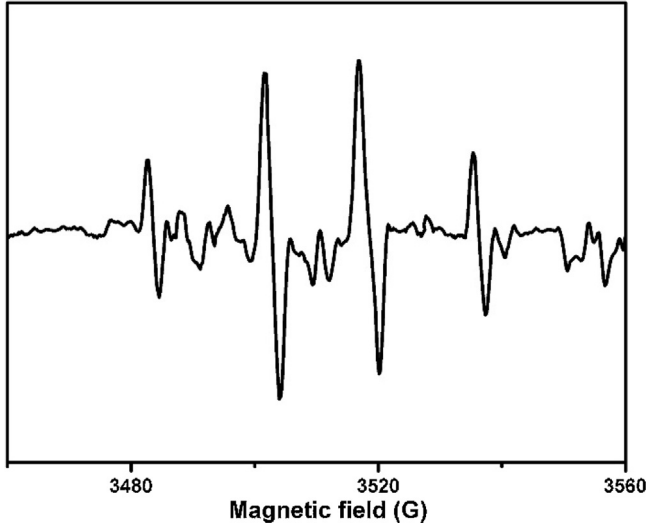


Fig. 6. DMPO spin-trapping ESR spectra of TC solution after UV irradiation.

a series of quenchers were employed to scavenge the relevant reactive species. As can be seen from Fig. 7, the addition of *tert*-butyl alcohol (TBA) [45], as a scavenger for hydroxyl radicals ($\cdot\text{OH}$) dramatically suppresses the photo-Fenton reaction. A similar inhibition phenomenon is also observed when the scavenger of silver nitrate (AgNO_3) for photogenerated electrons is added to the reaction system [46]. When the scavenger of *p*-benzoquinone for superoxide radical ($\cdot\text{O}_2^-$) is added, the degradation rate displays a slight decrease in the presence of *p*-benzoquinone (BQ) [47]. To evaluate the effect of dissolved oxygen on the removal efficiency of TC, the photo-Fenton-like reaction was conducted under N_2 protection (Fig. S11). The degradation ratio of TC is 89%, lower than that without N_2 . However, the effect of $\cdot\text{O}_2^-$ in the photo-Fenton-like process is negligible compared to $\cdot\text{OH}$. In addition, the introduction of ammonium oxalate (AO) as a scavenger for photogenerated holes (h^+) has no effect on the degradation of TC [48], suggesting that h^+ is not the directly reactive species responsible for TC degradation. Therefore, the hydroxyl radicals and electrons play an important role in the catalytic reaction.

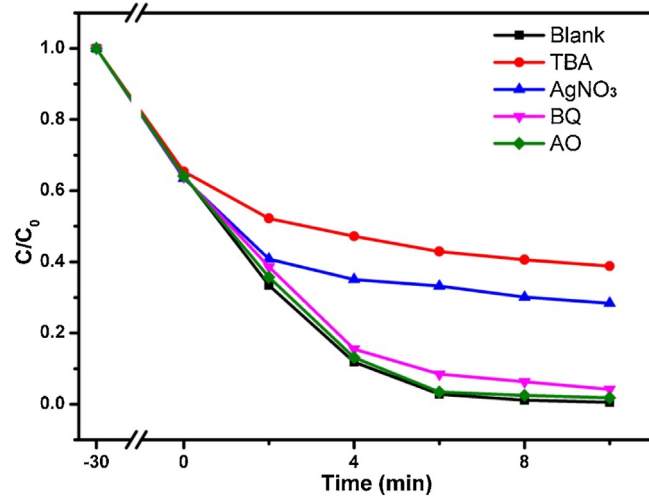
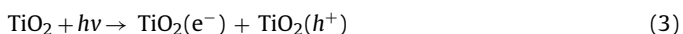
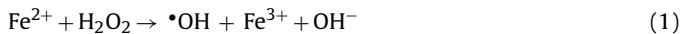
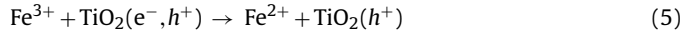


Fig. 7. Controlled experiments using different radical scavengers (0.1 mM) for the degradation of TC at room temperature and pH 3.



Based on the above results, The assumed mechanism is illustrated in Fig. 8 that TC is mainly degraded by $\cdot\text{OH}$ generated by different ways. $\cdot\text{OH}$ can be generated from the photo-Fenton-like process shown in Eq. (1) [49–51], the direct photolysis of H_2O_2 (Eq. (2)) and through the photocatalytic oxidation of adsorbed H_2O (Eqs. (3) and (4)) by holes in the valence band of TiO_2 surface. Compared with the naked Fe_3O_4 NPs, photo-induced electrons generated from TiO_2 can cause the reduction of Fe^{3+} to Fe^{2+} , benefitting from the good interaction between the TiO_2 shell and Fe_3O_4 core. Meanwhile, the photo-generated electrons and holes are more efficiently isolated (Eq. (5)) [52]. Moreover, for the yolk-shell structured $\text{Fe}_3\text{O}_4@\text{void}@\text{TiO}_2$, TC molecules can be effectively enriched into the cavity between Fe_3O_4 and TiO_2 NPs, which provides a microenvironment to confine the reactants. As such, TC molecules are instantly attacked by the concentrated $\cdot\text{OH}$, resulting in more efficient degradation than $\text{Fe}_3\text{O}_4@\text{TiO}_2$ and $\text{Fe}_3\text{O}_4@\text{SiO}_2@\text{TiO}_2$.

Moreover, we used the HPLC to test the concentration of TC. As shown in Fig. S12a, there is a slight increase of remnant TC determined by HPLC compared to UV-vis spectrophotometer. The degradation efficiency of TC on other materials were also determined. From Fig. S12b, all the degradation ratios of

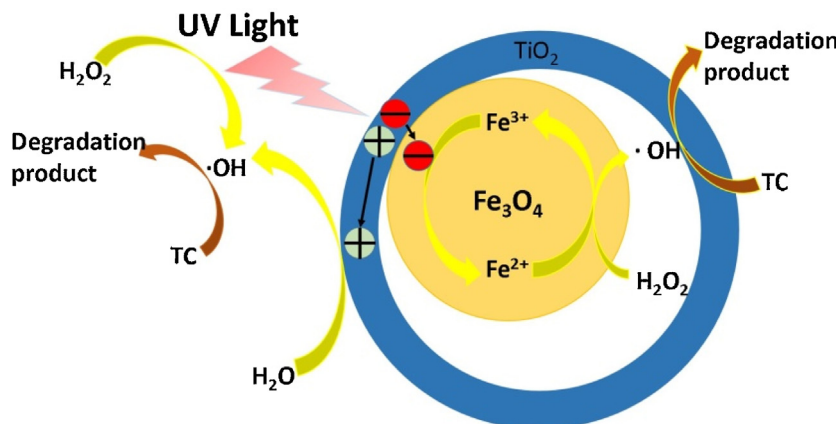


Fig. 8. Possible mechanism proposed for the photo-Fenton-like degradation for TC at room temperature.

TC evaluated by HPLC were lower than those from UV-vis spectrophotometer in the case of the same material. However, the $\text{Fe}_3\text{O}_4@\text{void}@\text{TiO}_2$ still shows the best performance, in line with the results detected by UV-vis spectrophotometer. To further test the activity of $\text{Fe}_3\text{O}_4@\text{void}@\text{TiO}_2$, it was also used as a photo-Fenton-like catalyst in the degradation of Methylene blue (MB), which can degrade MB totally within 18 min (Fig. S13), displaying a notable activity compared to other materials.

4. Conclusion

In summary, we have successfully synthesized the yolk-shell structured $\text{Fe}_3\text{O}_4@\text{void}@\text{TiO}_2$ through a sol-gel process and an ultrasound etching method. The $\text{Fe}_3\text{O}_4@\text{void}@\text{TiO}_2$ NPs with a high specific surface area and a well-defined hollow structure exhibit a remarkable performance for degrading TC due to the synergic effect between the TiO_2 shell and the Fe_3O_4 core. Furthermore, the catalyst can work in a wide pH range of 3–9. Owing to the high magnetization and good stability, the $\text{Fe}_3\text{O}_4@\text{void}@\text{TiO}_2$ can be conveniently isolated from the reaction solution and recycled for 5 times without significant loss of activity.

Acknowledgements

This work has been supported by National Nature Science Foundation of China (U140710223, 21237003 and 21377038), the National Basic Research Program of China (973 Program, 2013CB632403), the Science and Technology Commission of Shanghai Municipality (14ZR1410700, 14230710500 and 16JC1401400), Petro-China Innovation Foundation <gn3>2015D-5006-0402</gn3>, the Fundamental Research Funds for the Central Universities.

Appendix A. Supplementary data

Supplementary data associated with this article can be found, in the online version, at <http://dx.doi.org/10.1016/j.apcatb.2016.07.043>.

TEM images; Absorption spectra; Adsorption kinetic curve; Fitting curves of Langmuir models of the TC; Relation between zeta potential and solution pH of $\text{Fe}_3\text{O}_4@\text{void}@\text{TiO}_2$; FT-IR spectra; Catalytic behavior of the recycled $\text{Fe}_3\text{O}_4@\text{void}@\text{TiO}_2$ NPs; The study on iron leached from $\text{Fe}_3\text{O}_4@\text{void}@\text{TiO}_2$ catalyst; Efficiency changes of TOC removal within six cycles in the photo-Fenton-like process; Changes of TOC removal with time in the photo-Fenton-like degradation of TC; Catalytic behavior of the recycled $\text{Fe}_3\text{O}_4@\text{void}@\text{TiO}_2$ NPs.; Degradation kinetic of TC by different catalysts under pH

3; Photo-Fenton-like degradation of TC under N_2 atmosphere; Photo-Fenton-like degradation of TC monitored by UV-vis spectrophotometer and HPLC; Photo-Fenton-like degradation of TC by different materials monitored by UV-vis spectrophotometer and HPLC; Photo-Fenton-like degradation of MB; Thermodynamic constant for the adsorption performance of TC on $\text{Fe}_3\text{O}_4@\text{void}@\text{TiO}_2$; Pseudo-second-order kinetic parameters for TC adsorptions on $\text{Fe}_3\text{O}_4@\text{void}@\text{TiO}_2$. Eqs. (S1)–(S4).

References

- [1] F. Pérez, J.A. García-Hortal, X. Domènec, J. Peral, *Appl. Catal. B* 36 (2002) 63–74.
- [2] P. Bautista, A.F. Mohedano, J.A. Casas, J.A. Zazo, J.J. Rodriguez, *J. Chem. Technol. Biotechnol.* 83 (2008) 1323–1338.
- [3] V. Homem, L. Santos, *J. Environ. Manage.* 92 (2011) 2304–2347.
- [4] M. Klavarioti, D. Mantzavinos, D. Kassinos, *Environ. Int.* 35 (2009) 402–417.
- [5] B. Kakavandi, A. Taktadan, N. Jaafarzadeh, M. Azizi, A. Mirzaei, A. Azari, *J. Photochem. Photobiol. A: Chem.* 314 (2016) 178–188.
- [6] C. Reyes, J. Fernández, J. Freer, M.A. Mondaca, C. Zaror, S. Malato, H.D. Mansilla, *J. Photochem. Photobiol. A: Chem.* 184 (2006) 141–146.
- [7] E. Neyens, J. Baeyens, J. Hazard. Mater. 98 (2003) 33–50.
- [8] S. Caudo, G. Centi, C. Genovese, S. Perathoner, *Top. Catal.* 40 (2006) 207–219.
- [9] W.P. Kwan, B.M. Voelker, *Environ. Sci. Technol.* 37 (2003) 1150–1158.
- [10] S. Yang, H. He, D. Wu, D. Chen, X. Liang, Z. Qin, M. Fan, J. Zhu, P. Yuan, *Appl. Catal. B* 89 (2009) 527–535.
- [11] N. Jaafarzadeh, B. Kakavandi, A. Taktadan, R.R. Kalantary, M. Azizi, S. Jorf, *RSC Adv.* 5 (2015) 84718–84728.
- [12] Y. Kuang, Q. Wang, Z. Chen, M. Megharaj, R. Naidu, *J. Colloid Interface Sci.* 410 (2013) 67–73.
- [13] L. Xu, J. Wang, *Appl. Catal. B* 123–124 (2012) 117–126.
- [14] L. Xu, J. Wang, *Environ. Sci. Technol.* 46 (2012) 10145–10153.
- [15] Z. Ai, L. Lu, J. Li, L. Zhang, J. Qiu, M. Wu, *J. Phys. Chem. C* 111 (2007) 4087–4093.
- [16] X. Tan, L. Lu, L. Wang, J. Zhang, *Eur. J. Inorg. Chem.* 2015 (2015) 2928–2933.
- [17] X. Wang, H. Chen, *Colloids Surf. Physicochem. Eng. Aspects* 485 (2015) 25–33.
- [18] D. Wang, T. Hisatomi, T. Takata, C. Pan, M. Katayama, J. Kubota, K. Domen, *Angew. Chem. Int. Ed.* 52 (2013) 11252–11256.
- [19] Z.M. Cui, Z. Chen, C.-Y. Cao, L. Jiang, W.-G. Song, *Chem. Commun.* 49 (2013) 2332–2334.
- [20] T. Zeng, X. Zhang, S. Wang, Y. Ma, H. Niu, Y. Cai, *Chem. Eur. J.* 20 (2014) 6474–6481.
- [21] C. Liu, J. Li, J. Qi, J. Wang, R. Luo, J. Shen, X. Sun, W. Han, L. Wang, *ACS Appl. Mater. Interfaces* 6 (2014) 13167–13173.
- [22] J. Wang, W. Li, F. Wang, Y. Xia, A.M. Asiri, D. Zhao, *Nanoscale* 6 (2014) 3217–3222.
- [23] W. Zhou, Y. Yu, H. Chen, F.J. DiSalvo, H.D. Abruna, *J. Am. Chem. Soc.* 135 (2013) 16736–16743.
- [24] J. Liu, S.Z. Qiao, S. Budi Hartono, G.Q. Lu, *Angew. Chem. Int. Ed.* 49 (2010) 4981–4985.
- [25] Y. Chen, H. Chen, L. Guo, Q. He, F. Chen, J. Zhou, J. Feng, J. Shi, *ACS Nano* 4 (2010) 529–539.
- [26] J. Yang, D. Shen, L. Zhou, W. Li, X. Li, C. Yao, R. Wang, A.M. El-Toni, F. Zhang, D. Zhao, *Chem. Mater.* 25 (2013) 3030–3037.
- [27] P. Rai, J.-W. Yoon, H.-M. Jeong, S.-J. Hwang, C.-H. Kwak, J.-H. Lee, *Nanoscale* 6 (2014) 8292–8299.
- [28] C. Wang, L. Yin, L. Zhang, L. Kang, X. Wang, R. Gao, *J. Phys. Chem. C* 113 (2009) 4008–4011.
- [29] B. Cui, H. Peng, H. Xia, X. Guo, H. Guo, *Sep. Purif. Technol.* 103 (2013) 251–257.

- [30] J. Liu, Z. Sun, Y. Deng, Y. Zou, C. Li, X. Guo, L. Xiong, Y. Gao, F. Li, D. Zhao, *Angew. Chem. Int. Ed.* 48 (2009) 5875–5879.
- [31] W. Li, Y. Deng, Z. Wu, X. Qian, J. Yang, Y. Wang, D. Gu, F. Zhang, B. Tu, D. Zhao, *J. Am. Chem. Soc.* 133 (2011) 15830–15833.
- [32] W. Li, J. Yang, Z. Wu, J. Wang, B. Li, S. Feng, Y. Deng, F. Zhang, D. Zhao, *J. Am. Chem. Soc.* 134 (2012) 11864–11867.
- [33] W. Stöber, A. Fink, E. Bohn, *J. Colloid Interface Sci.* 26 (1968) 62–69.
- [34] S. Liu, F. Lu, R. Xing, J.J. Zhu, *Chem. Eur. J.* 17 (2011) 620–625.
- [35] H. Liu, W. Li, D. Shen, D. Zhao, G. Wang, *J. Am. Chem. Soc.* 137 (2015) 13161–13166.
- [36] V. Fischer, I. Lieberwirth, G. Jakob, K. Landfester, R. Muñoz-Espí, *Adv. Funct. Mater.* 23 (2013) 451–466.
- [37] J. Zhang, B. Li, W. Yang, J. Liu, *Ind. Eng. Chem. Res.* 53 (2014) 10629–10636.
- [38] T. Heberer, *Toxicol. Lett.* 131 (2002) 5–17.
- [39] Y. Gao, Y. Li, L. Zhang, H. Huang, J. Hu, S.M. Shah, X. Su, *J. Colloid Interface Sci.* 368 (2012) 540–546.
- [40] I.K. Konstantinou, T.A. Albanis, *Appl. Catal. B* 49 (2004) 1–14.
- [41] S. Patil, A. Sandberg, E. Heckert, W. Self, S. Seal, *Biomaterials* 28 (2007) 4600–4607.
- [42] J. Sun, S. Zhou, P. Hou, Y. Yang, J. Weng, X. Li, M. Li, *J. Biomed. Mater. Res. A* 80A (2007) 333–341.
- [43] D. Grenier, M.-P. Huot, D. Mayrand, *Antimicrob. Agents Chemother.* 44 (2000) 763–766.
- [44] J.J. López-Peña, M. Sánchez-Polo, C.V. Gómez-Pacheco, J. Rivera-Utrilla, *J. Chem. Technol. Biotechnol.* 85 (2010) 1325–1333.
- [45] Y. Lin, D. Li, J. Hu, G. Xiao, J. Wang, W. Li, X. Fu, *J. Phys. Chem. C* 116 (2012) 5764–5772.
- [46] A. Kudo, K. Ueda, H. Kato, I. Mikami, *Catal. Lett.* 53 (1998) 229–230.
- [47] P.S. Rao, E. Hayon, *Biochem. Biophys. Res. Commun.* 51 (1973) 468–473.
- [48] X. Pan, Y.J. Xu, *J. Phys. Chem. C* 117 (2013) 17996–18005.
- [49] J.J. Pignatello, *Environ. Sci. Technol.* 26 (1992) 944–951.
- [50] M. Pera-Titus, V. García-Molina, M.A. Baños, J. Giménez, S. Esplugas, *Appl. Catal. B* 47 (2004) 219–256.
- [51] R. Bauer, G. Waldner, H. Fallmann, S. Hager, M. Klare, T. Krutzler, S. Malato, P. Maletzky, *Catal. Today* 53 (1999) 131–144.
- [52] G. Li, Z. Tang, *Nanoscale* 6 (2014) 3995–4011.